Available online at www.sciencedirect.com
ScienceDirect
Trans. Nonferrous Met. Soc. China 33(2023) 1345−1360
Transactions of Nonferrous Metals Society of China
www.tnmsc.cn

Numerical simulation of squeeze casting of aluminum alloy flywheel housing with large wall thickness difference and complex shape

Ju-fu JIANG[1], Ning GE[1], Min-jie HUANG[1], Ming-xing LI[1], Ying WANG[2], Chang-jie DING[3], De-chao ZOU[3]

1. School of Materials Science and Engineering, Harbin Institute of Technology, Harbin 150001, China;
2. School of Mechatronics Engineering, Harbin Institute of Technology, Harbin 150001, China;
3. Dalian Innovation Die-casting Co., Ltd., Dalian 116600, China

Received 25 January 2022; accepted 24 May 2022

Abstract: The squeeze casting process of ZL104 aluminum alloy flywheel housing with large wall thickness difference and complex shape was simulated by ProCAST software. The results show that the filling process was stable and could be divided into four stages: connection of channels, filling of horizontal zone, vertical direction, and difficult-filling zone. There were six characteristic zones with solidification lag, where shrinkage cavity and shrinkage porosity were obvious. The location prediction of defects was accurate. Through range analysis of defects volume, the optimal combination of process parameters was determined as pouring temperature of 650 ℃, specific pressure of 48 MPa, mold temperature of 220 ℃, local specific pressure of 800 MPa, and pressure delay time of 10 s (Side *A*) and 12 s (Side *B*). The maximum stress occurred in the thin-walled structure with fast solidification and large curvature. The simulation results were verified by the actual process.

Key words: numerical simulation; squeeze casting; large wall thickness difference; complex shape; local pressure

1 Introduction

Squeeze casting is an economical and feasible method to manufacture aluminum alloy parts with high mechanical properties and dense microstructure, which combines the characteristics of casting and forging [1−3]. The process of mold filling, solidification, and feeding can be completed under pressure, to achieve the purpose of smooth filling, refining grains, improving microstructure, and controlling casting defects. In recent years, the development of numerical simulation technology has provided new ideas for the development and process design of squeeze casting products [4−9]. HU et al [10] introduced a mathematical model of particle reinforced metal matrix composites and applied it to the mold filling and particle flow simulation of castings. SUN et al [11] combined MAGMASOFT software and squeeze casting tests to determine the heat transfer coefficient in the squeeze casting process of A443 aluminum alloy. KIM and KANG [12] studied the feasibility of applying finite element simulation in the rheological squeeze casting of A356 aluminum alloy complex components with high solid fraction and predicted the possible defects through simulation and experiment. LI et al [13] simulated the squeeze casting of gearbox cover by ProCAST software, and accurately predicted and verified the locations of shrinkage cavity and shrinkage porosity defects in actual production.

The importance of numerical simulation is reflected in simulation and prediction, which is the most efficient means to predict defects in advance and then take corresponding measures to eliminate

Corresponding author: Ju-fu JIANG, Tel: +86-18746013176, E-mail: jiangjufu@hit.edu.cn;
Ying WANG, Tel: +86-15945697615, E-mail: wangying1002@hit.edu.cn
DOI: 10.1016/S1003-6326(23)66187-4

defects. At present, for squeeze casting parts with small size, simple shape, and conventional wall thickness, numerical simulation can effectively shorten the development time and reduce the cost. Meanwhile, there are mature approaches to overcome the predicted defects. LI et al [14] used MAGMASOFT software to simulate the squeeze casting of the automobile control arm, accurately predicted the locations of hot spots in the solidification process, and overcame the occurrence of shrinkage defects by local pressure supplement and cooling line setting.

However, for large, complex, and uneven wall thickness squeeze casting parts, such as the large-sized flywheel housing in this study, as a typical engine system part with a large wall thickness difference and complex shape, it is still difficult to eliminate the defects. Therefore, simulation of the solidification process and accurate prediction of defect locations are very important for taking effective methods to reduce the detrimental effect of defects during mold design and squeeze casting process.

In this study, 18 groups of numerical simulations were carried out on the squeeze casting process of ZL104 aluminum alloy flywheel housing with a large wall thickness difference and complex shape by using ProCAST software. The filling order, solidification rule, displacement field, stress distribution, and the locations of defects were analyzed. Range analysis of the volume contents of defects in 18 groups of simulations was carried out to obtain the optimal combination of process parameters. In addition, the actual process was validated. It was significant to provide technical support for the process design and optimization of subsequent actual squeeze casting production.

2 Preprocess

2.1 Mathematical models for simulation

The indirect squeeze casting process mainly involves two stages: mold filling and solidification under pressure. It is a complex physical and chemical process. The simulation can be simplified using the following hypotheses.

(1) The molten alloy is an incompressible Newtonian fluid.

(2) The thermophysical parameters of casting and mold materials are related to temperature.

(3) The heat-transfer process is dominated by heat conduction during solidification, convection and radiation parts are ignored.

(4) The pressure exerted by squeeze casting can immediately eliminate the air gap between casting and mold. The equivalent interface heat transfer coefficient (IHTC) reaches the peak value instantaneously and decreases linearly with solidification shrinkage until the end of pressure holding.

(5) The constitutive model of stress calculation is the thermal elastoplastic model. The materials are isotropic, and the hardening model is the linear hardening model.

2.1.1 Governing equations during mold filling

The flow of alloy melt during mold filling is equivalent to the unsteady flow of an incompressible viscous liquid [15]. It obeys the laws of conservation of mass and momentum, and can thus be described by continuity equation (Eq. (1)) and Navier-Stokes equation (Eq. (2)) [16,17].

VOF method was adopted to track the position and movement of the free surface by solving a set of continuity and Navier-Stokes equations. In this method, the filling state of the fluid is described by volume fraction (f), which is defined as the ratio of fluid (target fluid) volume to mesh volume. f=0 indicates that the mesh does not contain fluid. f=1 indicates that the mesh is filled with fluid and when $0<f<1$, it indicates the presence of fluid but not full, that is, the position of the free surface. When tracking free surface, the governing equation is volume fraction (Eq. (3)) [18]. The calculation of the temperature field satisfies the energy conservation (Eq. (4)) [19]. The above equations are all mathematical forms in the rectangular coordinate system.

$$\frac{\partial u}{\partial x}+\frac{\partial v}{\partial y}+\frac{\partial w}{\partial z}=0 \tag{1}$$

$$\rho\left(\frac{\partial V_i}{\partial t}+\frac{\partial V_i}{\partial x}+\frac{\partial V_i}{\partial y}+\frac{\partial V_i}{\partial z}\right)=-\nabla p+\rho F_i+\gamma\nabla^2 V_i \tag{2}$$

$$\frac{\partial f}{\partial t}+u\frac{\partial f}{\partial x}+v\frac{\partial f}{\partial y}+w\frac{\partial f}{\partial z}=0 \tag{3}$$

$$\begin{aligned}&\frac{\partial}{\partial t}\left(\rho C_p T\right)+\frac{\partial}{\partial t}\left(\rho C_p uT\right)+\\&\quad\frac{\partial}{\partial t}\left(\rho C_p vT\right)+\frac{\partial}{\partial t}\left(\rho C_p wT\right)=\\&\quad\frac{\partial}{\partial x}\left(\lambda\frac{\partial T}{\partial x}\right)+\frac{\partial}{\partial y}\left(\lambda\frac{\partial T}{\partial y}\right)+\frac{\partial}{\partial z}\left(\lambda\frac{\partial T}{\partial z}\right)+Q\end{aligned} \tag{4}$$

where ρ is the density of the fluid, p is the internal pressure of the fluid, γ is the kinematic viscosity, V_i is the component of velocity vectors (u, v, w) in x, y, z directions at a specific time t, ∇^2 is the Laplace operator, ∇ is the gradient mark, F_i is the projection of unit mass force in the x, y, z directions, C_p is the specific heat at constant pressure, T is the temperature, λ is the thermal conductivity, and Q is the heat source.

2.1.2 Governing equations during solidification

Solidification is a complex physical and chemical process. According to the previous hypothesis, heat transfer between casting and mold is dominated by heat conduction in the squeeze casting process. The mathematical model of temperature field simulation is Fourier partial differential equation (Eq. (5)) [20,21].

$$\frac{\partial}{\partial t}\left(\rho C_p T\right)=\frac{\partial}{\partial x}\left(\lambda\frac{\partial T}{\partial x}\right)+\frac{\partial}{\partial y}\left(\lambda\frac{\partial T}{\partial y}\right)+\frac{\partial}{\partial z}\left(\lambda\frac{\partial T}{\partial z}\right)+Q \tag{5}$$

Q is related to the latent heat of crystallization which can be expressed as [22]

$$Q=\rho L\frac{\partial f_s}{\partial T}\frac{\partial T}{\partial t} \tag{6}$$

where L is the latent heat, and f_s is the volume fraction of solid state.

ProCAST software used the enthalpy method to deal with latent heat. The method used the relationship between enthalpy and temperature during phase transition to calculate it iteratively. The enthalpy (H) is defined as [23]

$$H(T)=\int_0^T C(T)\mathrm{d}T+L(1-f_s) \tag{7}$$

Here, $C(T)$ is a function of temperature. The derivative of Eq. (7) to temperature was substituted into Eq. (5) to obtain Eq. (8) [24]

$$\rho\frac{\partial H(T)}{\partial t}=\frac{\partial}{\partial x}\left(\lambda\frac{\partial T}{\partial x}\right)+\frac{\partial}{\partial y}\left(\lambda\frac{\partial T}{\partial y}\right)+\frac{\partial}{\partial z}\left(\lambda\frac{\partial T}{\partial z}\right) \tag{8}$$

During solidification, the alloy goes through three stages: liquid state, solid−liquid state, and solid state. When the alloy is completely in liquid state, the temperature field has no effect on the stress distribution. When the alloy is in liquid−solid state and solid state, there is a thermal-mechanical coupling effect. According to the previous hypothesis, for the thermal elastoplastic theory model, the strain increment can be written as follows [25,26]:

$$\mathrm{d}\varepsilon=\mathrm{d}\varepsilon_{\mathrm{el}}+\mathrm{d}\varepsilon_{\mathrm{t}}+\mathrm{d}\varepsilon_{\mathrm{pl}} \tag{9}$$

where $\mathrm{d}\varepsilon$ is the total strain increment, $\mathrm{d}\varepsilon_{\mathrm{el}}$ is the elastic strain increment, $\mathrm{d}\varepsilon_{\mathrm{t}}$ is the thermal strain increment related to the coefficient of thermal expansion, and $\mathrm{d}\varepsilon_{\mathrm{pl}}$ is the plastic strain increment.

The influence of temperature on the physical parameters of materials is taken into account. The stress increment is expressed as [25]

$$\mathrm{d}\sigma=\boldsymbol{D}_{\mathrm{ep}}(\mathrm{d}\varepsilon-\mathrm{d}\varepsilon_{\mathrm{t}}-\mathrm{d}\varepsilon_0)+\mathrm{d}\sigma_0 \tag{10}$$

where $\boldsymbol{D}_{\mathrm{ep}}$ is the elastoplastic matrix related to the elastic modulus, plastic modulus, and Poisson's ratio, $\mathrm{d}\varepsilon_0$ is the additional strain affected by temperature, and $\mathrm{d}\sigma_0$ is the additional stress influenced by temperature.

For the prediction of solidification defects, ProCAST software used the Niyama criterion (Eq. (11)) [27] to predict solidification shrinkage and porosity.

$$G/\sqrt{R}=C_{\mathrm{Niyama}} \tag{11}$$

where C_{Niyama} is the critical criterion value, G is the temperature gradient, and R is the solidification rate.

2.2 Model building

Unigraphics NX was used to build three-dimensional models of a large-sized flywheel housing and squeeze casting mold, as shown in Figs. 1 and 2, respectively. The outline size of the flywheel housing was 576 mm × 547 mm × 184 mm, the mass was 20.4 kg, the maximum wall thickness was 56 mm, and the thinnest wall thickness was 6 mm. The mold was simplified into three parts: lower mold (Fig. 2(a)), upper mold (Fig. 2(b)), and slide block (Fig. 2(c)). Three-dimensional models were imported into ProCAST software for mesh division. The inner and outer surface mesh side lengths were respectively planned to be 4 and 20 mm by considering the calculation accuracy and calculation time comprehensively. And the more complex parts of the local structures were further refined. The total numbers of surface meshes and volume meshes were 220826 and 4273986, respectively. Figure 3 shows the schematic diagram of mold and cavity mesh division.

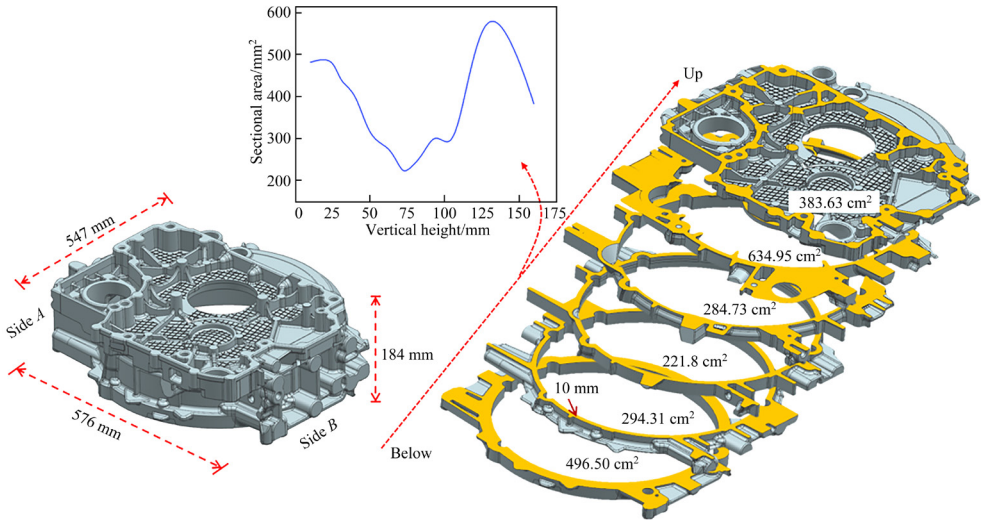

Fig. 1 Three-dimensional model of flywheel housing

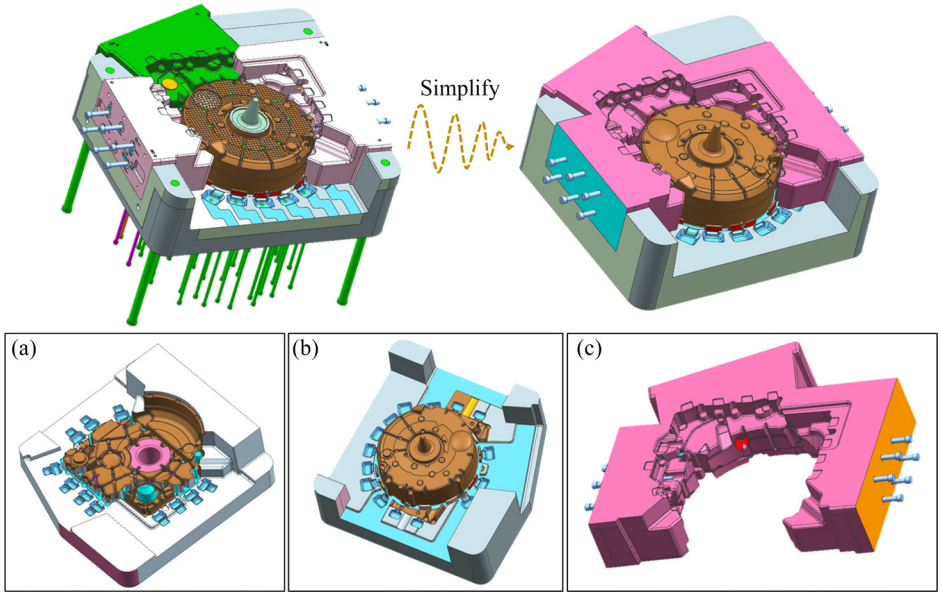

Fig. 2 Pre- and post-simplification of 3D mold model: (a) Lower mold; (b) Upper mold; (c) Slide block

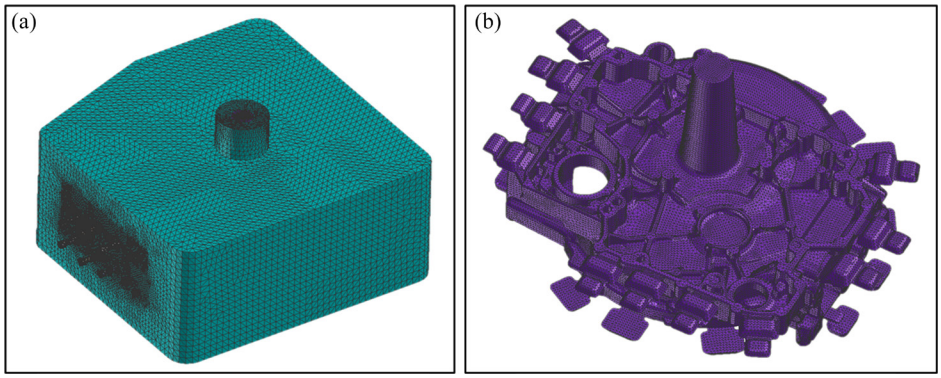

Fig. 3 Mesh division of squeeze casting flywheel housing mold (a) and cavity (b)

2.3 Physical and process parameters

ZL104 aluminum alloy was used as the material, and H13 steel was used as the mold material in the simulation. The fluid parameters and physical parameters used herein were all obtained from the material database of ProCAST software.

The solidus and liquidus temperatures of ZL104 aluminum alloy are 546 and 600 °C, respectively. Figure 4 shows the variation curves of various parameters of ZL104 aluminum alloy with temperature.

In this study, process parameters included pouring temperature, mold temperature, specific pressure, local specific pressure, delay time, pressure holding time, and filling time.

The accurate determination of interface heat transfer coefficients (IHTC) between casting and mold is a very difficult task since it depends on numerous factors, such as specific pressure, melt temperature, mold temperature, formation of the air gap, and geometry. In squeeze casting process, the casting–mold interface heat transfer coefficients (IHTC) are primarily affected by the specific pressure levels, and other factors have little effect on IHTC after the pressure was applied, as reported previously [28]. The equivalent interface heat transfer coefficient of parts and molds can be used to indirectly reflect the effect of pressure [29,30]. And the specific pressures and the peak values of the equivalent interface heat transfer coefficient meet the empirical formula [24,31,32], as shown in Eq. (12). Assuredly, further work is needed on experimentally determining an accurate relationship between the heat transfer coefficients and the specific pressure levels for ZL104 aluminum alloy squeeze casting.

$$h_{pv}=1990.5+94.8P \quad (12)$$

where h_{pv} is the peak value of the equivalent interface heat transfer coefficient (IHTC), and P is the specific pressure.

The research results of WANG et al [24] show that the equivalent interface heat transfer coefficient reached its peak value as soon as the pressure was

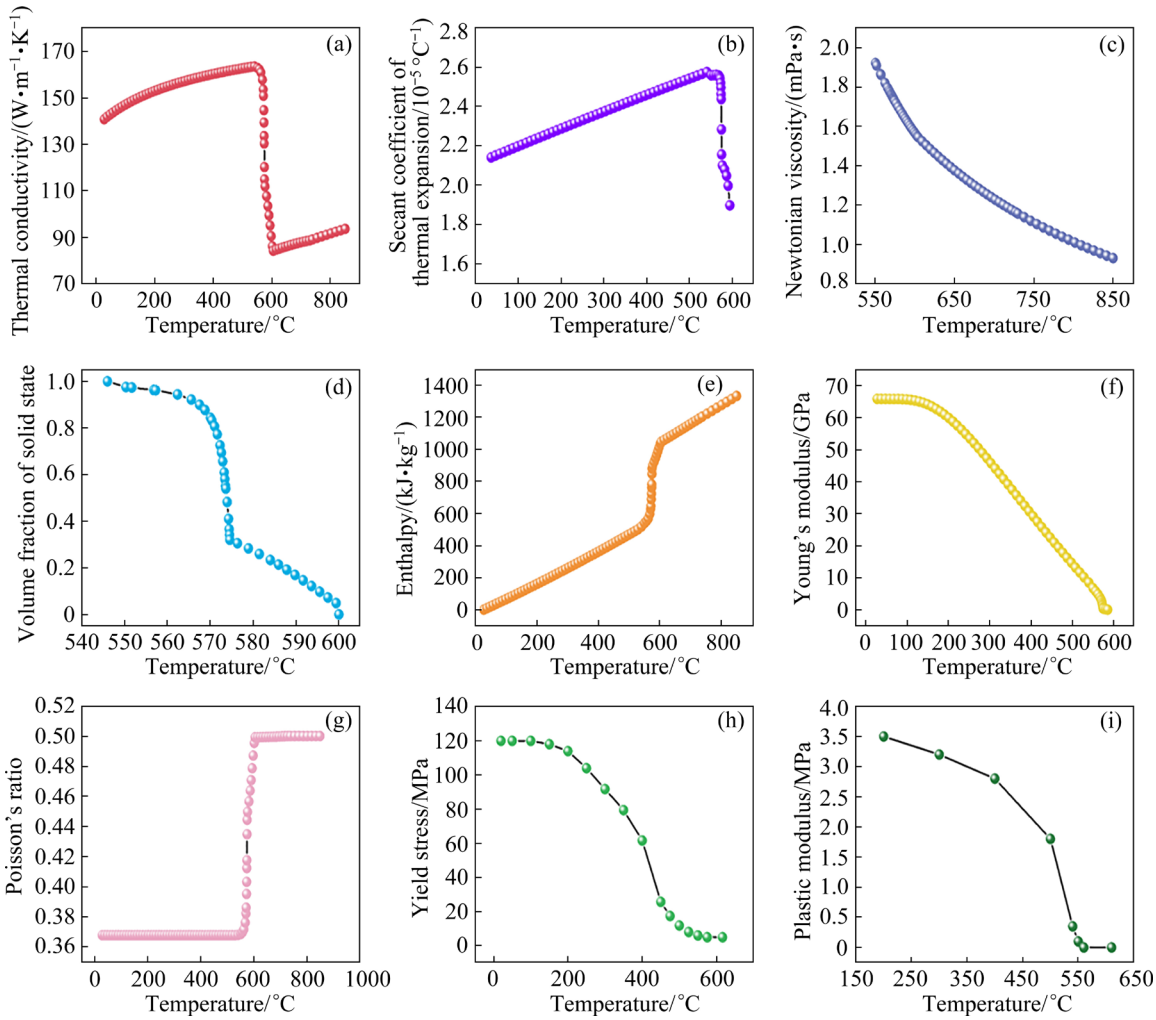

Fig. 4 Variation curves of thermal conductivity (a), secant coefficient of thermal expansion (b), Newtonian viscosity (c), volume fraction of solid state (d), enthalpy (e), Young's modulus (f), Poisson's ratio (g), yield stress (h), and plastic modulus (i) of ZL104 aluminum alloy with temperature

applied. And then the close contact formerly achieved between the casting and mold deteriorated with the occurrence of solidification shrinkage during the solidification process, and IHTC decreased [24]. As assumed previously, IHTC decreased linearly until the end of pressure holding, (h=2000 W·m^{-2}·℃$^{-1}$)

The peak values of the estimated equivalent interfacial heat transfer coefficients (IHTC) corresponding to different specific pressures are shown in Table 1. The process parameters in numerical simulation are shown in Table 2, and total simulation schemes are shown in Table 3. In ProCAST software, the variation curve of equivalent interfacial heat transfer coefficients (IHTC) with time can be set to realize the difference in delay time between Side *A* and Side *B*.

3 Simulation results and discussion

3.1 Flow field and temperature field during filling

Several characteristic time points were selected to express and analyze the flow field and temperature field in the filling process of squeeze casting by taking No.3 component (pouring temperature of 650 ℃, mold temperature of 220 ℃, specific pressure of 48 MPa, local specific pressure of 800 MPa, delay time of 15 s and 17 s) as an example. For the convenience of description, the directions of the component were named *A*, *B*, *C*, and *D* respectively, as shown in Fig. 5(a).

Table 1 Relationship between peak values of estimated equivalent interfacial heat transfer coefficient (IHTC) and specific pressure

Specific pressure/MPa	IHTC/(W·m^{-2}·℃$^{-1}$)
32	5024.1
40	5782.5
48	6540.9

Table 2 Process parameters in numerical simulation

Processing parameter	Value
Pouring temperature/℃	650, 658, 665
Mold temperature/℃	190, 210, 220
Specific pressure/MPa	32, 40, 48
Local specific pressure/MPa	0, 800
Delay time on Side *A*/s	10, 13, 15
Delay time on Side *B*/s	12, 15, 17
Pressure holding time/s	25
Filling time/s	5

Table 3 Total orthogonal simulation schemes

Serial number	Pouring temperature/℃	Specific pressure/MPa	Mold temperature/℃	Local specific pressure/MPa	Delay time/s
1	650	32	190	0	10(Side *A*); 12(Side *B*)
2	650	40	210	800	13(Side *A*); 15(Side *B*)
3	650	48	220	800	15(Side *A*); 17(Side *B*)
4	658	32	190	800	13(Side *A*); 15(Side *B*)
5	658	40	210	800	15(Side *A*); 17(Side *B*)
6	658	48	220	0	10(Side *A*); 12(Side *B*)
7	665	32	210	0	15(Side *A*); 17(Side *B*)
8	665	40	220	800	10(Side *A*); 12(Side *B*)
9	665	48	190	800	13(Side *A*); 15(Side *B*)
10	650	32	220	800	13(Side *A*); 15(Side *B*)
11	650	40	190	0	15(Side *A*); 17(Side *B*)
12	650	48	210	800	10(Side *A*); 12(Side *B*)
13	658	32	210	800	10(Side *A*); 12(Side *B*)
14	658	40	220	0	13(Side *A*); 15(Side *B*)
15	658	48	190	800	15(Side *A*); 17(Side *B*)
16	665	32	220	800	15(Side *A*); 17(Side *B*)
17	665	40	190	800	10(Side *A*); 12(Side *B*)
18	665	48	210	0	13(Side *A*); 15(Side *B*)

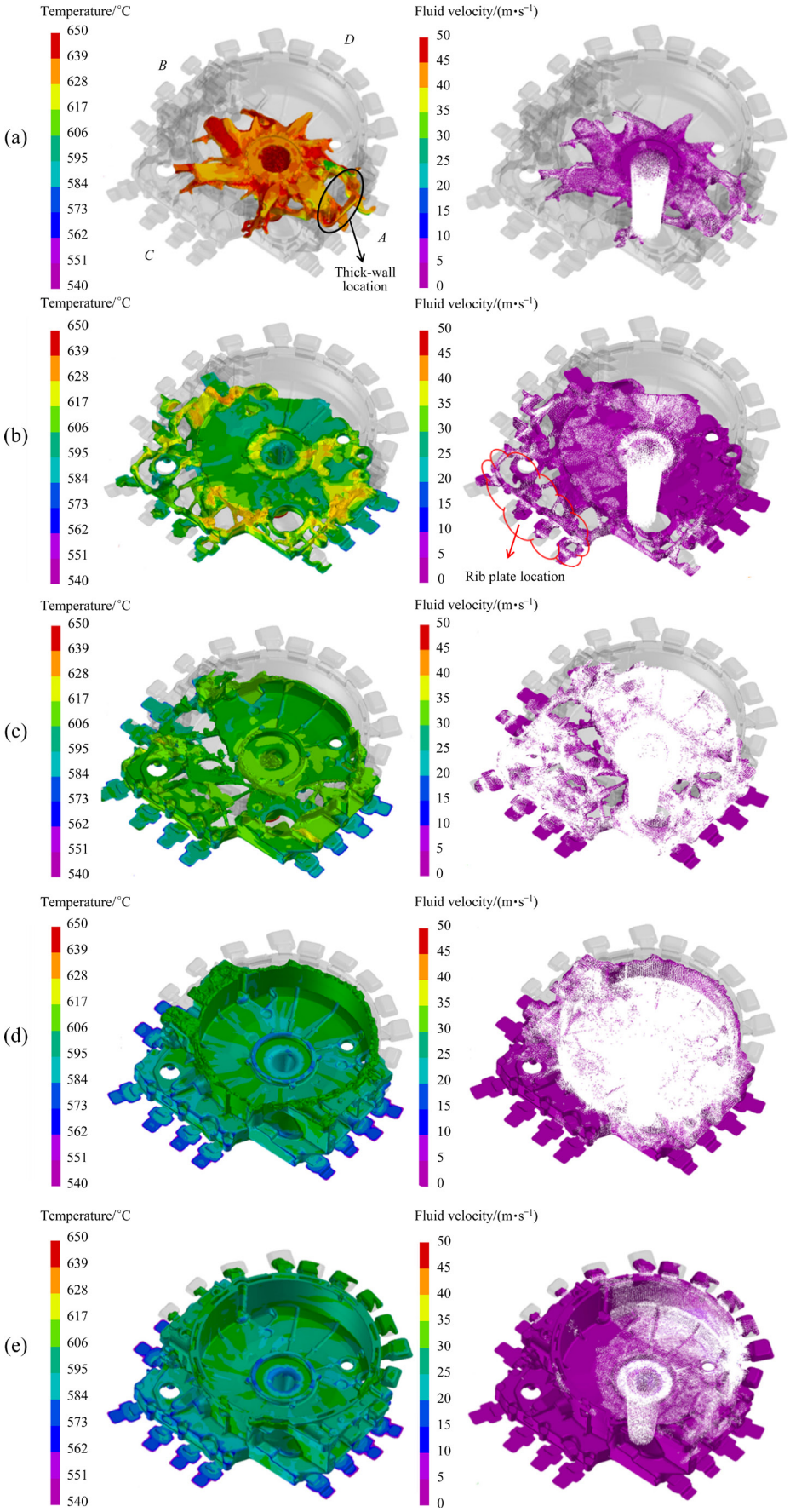

Fig. 5 Filling process of squeeze casting of No.3 component at 1.0 s (a), 2.0 s (b), 2.6 s (c), 4.2 s (d), and 4.8 s (e)

The molten alloy flowed into the mold cavity with reverse filling from the sprue, and then the mold cavity was filled in horizontal and vertical directions at the mold joint and the annular sidewall. The structure of the mold joint was complex, and the rib plate below it first completed the reverse filling and acted as a channel to transport the melt to the far end, as shown in Fig. 5(a). After filling for 1.0 s, the leading melt flowed from center to all around with less temperature loss. At 2.0 s, the melt in the channel of the rib was connected and the filling of the rib was completed. The temperature was close to the liquidus temperature, as shown in Fig. 5(b). The molten alloy flowed in a wide range in the form of a vortex, resulting in melt replacement. The melt temperature in the thick part was relatively high, as shown in Fig. 5(c). The horizontal filling was completed and the leading melt front flowed to multiple overflow grooves which played the role of collecting the low-temperature alloy liquid with more bubbles and slags. After 2.6 s of mold filling, the melt began to fill in the vertical direction, the rising liquid surface was basically flat, while the liquid surface on Side *D* was slightly ahead due to its simple structure, as shown in Fig. 5(d). The final stage was filling of the difficult-to-fill zone, which required higher pressure, velocity, and liquid transfer in a larger range for local filling. At 4.8 s, the main part of the flywheel housing was fully filled, as shown in Fig. 5(e). At 5.0 s, the overflow grooves were filled at the latest. XU and YING [33] pointed out that a reasonable filling velocity range should be set in the filling process. When the filling velocity is low, the filling process is slow, and the forefront of the liquid metal is rapidly cooled. Complex castings easily lead to defects of misrun, and the long filling time also reduces the processing efficiency. When the filling velocity is relatively high, the turbulence of liquid metal is strong, which easily leads to gas trapping and slag inclusion. During the whole filling stage of this study, the filling velocity was kept within a reasonable range, which can avoid gas trapping and slag inclusion to a certain extent.

As shown in Fig. 6, the average temperature of the free surface decreased with the increase of the filling time in the filling process, the cooling rate increased at first and then decreased, and gradually flattened, which was consistent with the rule of the temperature curve in the simulation results of ZHANG and CANTOR [31] and FARDI-ILKHCHY et al [34]. This was because in the horizontal direction, the free surface area for filling was large and the cooling rate was fast, while in the height direction, it was small and the cooling rate was slow. Meanwhile, the results also indicated that the pressure action of squeeze casting could eliminate the air gaps between the flowing melt and the mold surface in the conventional gravity casting process, and the bulk liquid turbulence existed in the locations where fluctuations occurred in the temperature curve [34]. The analysis of the average temperature change of the free liquid surface could support the stage division of the filling process.

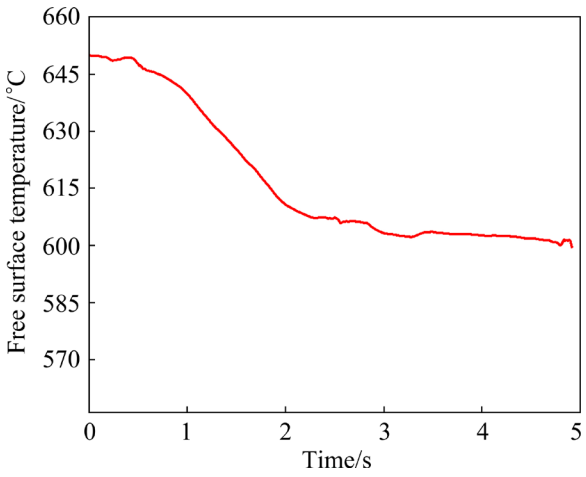

Fig. 6 Average temperature of free surface curve with time

To sum up, the filling process could be divided into four stages: connection of small resistance channels, filling of horizontal zone with large resistance, filling of vertical direction, and filling of difficult-filling zone. The filling order of different simulation schemes basically conformed to the above four stages. The overall filling process was relatively stable with very few local velocity fluctuations, and the filling velocity was basically stable at a low level. Combined with the pressure action of squeeze casting, the generation of gas trapping and slag inclusion can be reduced to a certain extent. The free liquid surface could gradually rise from bottom to top, and the cold front and the impurities in the mold cavity were discharged from the overflow grooves, which can effectively improve the product quality. At the end of the filling, the solid fraction was at a low level and the temperature distribution was uniform.

3.2 Temperature field during solidification

By analyzing the temperature field in the solidification process of the No. 3 component as shown in Fig. 7(a), it was found that the overall solidification rule was sequential solidification from outside to inside and from top to bottom.

At the early stage of solidification process, it could be observed that the upper and lower overflow grooves had the fastest cooling rate. The solidification process in Zone *D* was ahead of that in other zones. This was because that Zone *D* had thinner wall and simpler plane, less heat, and a larger contact area for effective heat transfer. The cooling rate was slow on Sides *A*, *B*, and local parts of Side *C*, where Sides *A* and *B* were concentrated in three thick-walled locations named as *A*-1−*A*-3 and *B*-1−*B*-3 respectively, while local parts of Side *C* were named as *C*-0, *C*-1 and *C*-2, respectively. These locations had obvious similarity that the shapes and structures were complex and the volumes were relatively large. Simultaneous solidification was not realized on Sides *A* and *B*. Therefore, they were relatively dangerous zones, which were prone to shrinkage cavity and shrinkage porosity defects, and needed to be focused on. At the later stage of solidification process, the heat transfer was hindered by the increase in local mold temperature, so the solidification time at these positions was longer. Obviously, the solidification time of the sprue was the longest.

Multiple characteristic points were selected from the above six characteristic zones to monitor the change in temperature with time. Locations of points are shown in Fig. 7(a). From Fig. 8(a), it can be observed that except for Zone *D*, where the solidification was the fastest, the temperature of other zones remained stable for a period of time, because the transferred heat could be supplemented

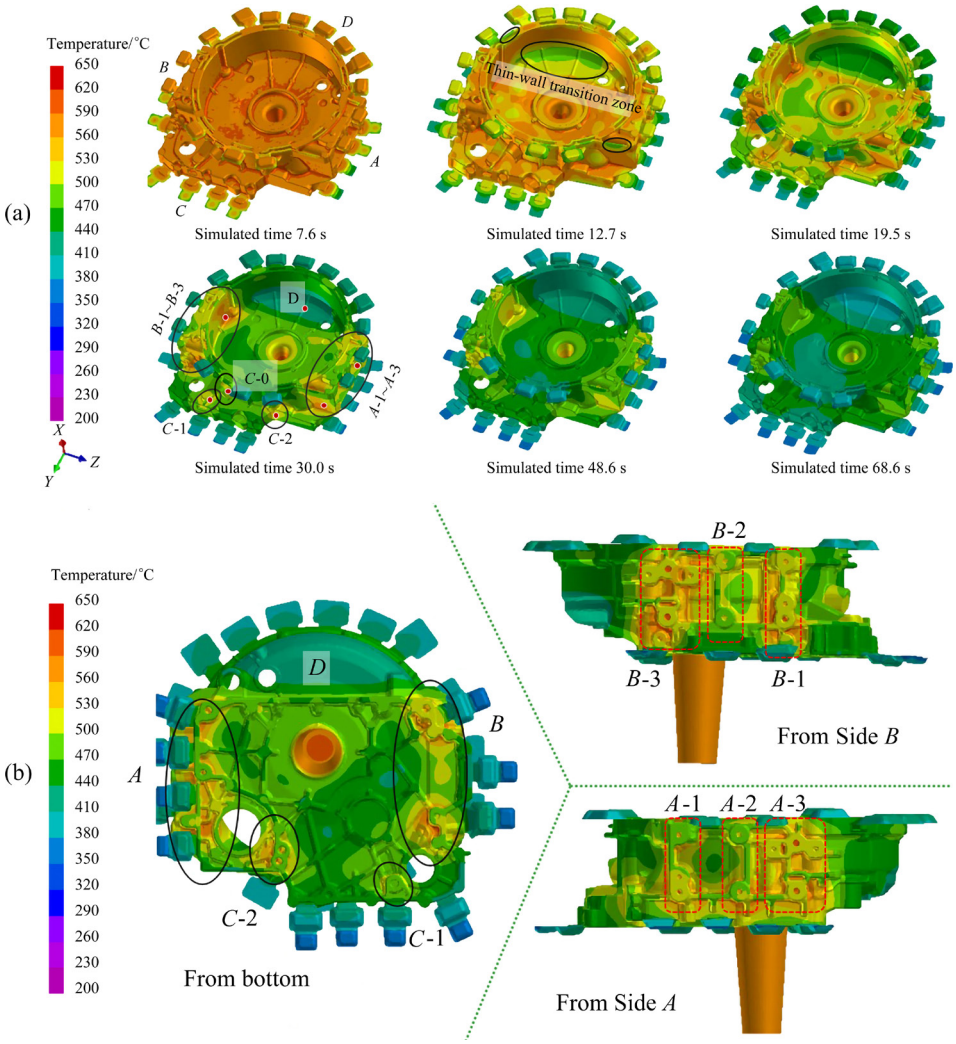

Fig. 7 Solidification process of No.3 component: (a) Temperature field; (b) Solidification state under different perspectives after 30 s simulation

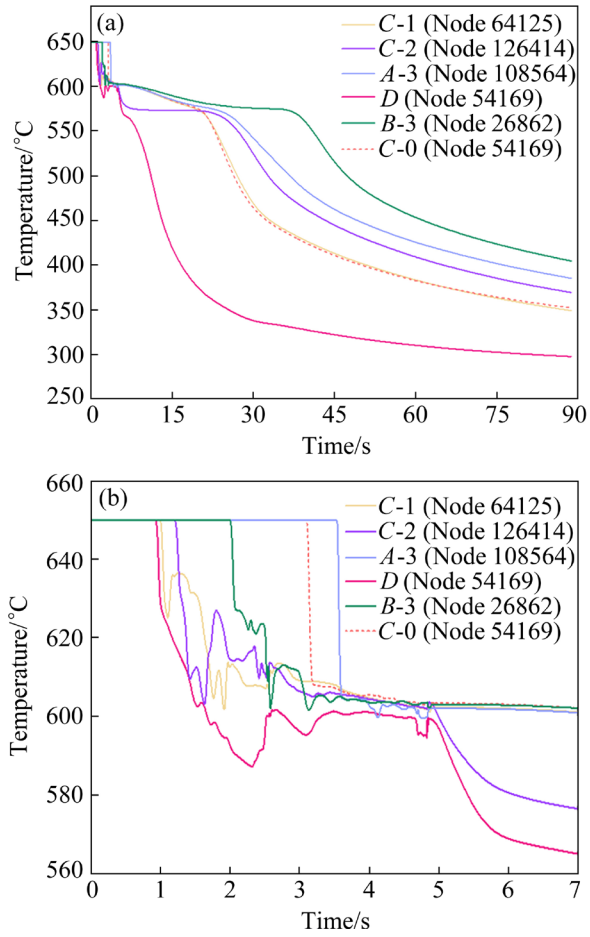

Fig. 8 Temperature variation curves of six characteristic points: (a) Temperature variation curves of whole process; (b) Short-time temperature variation curves

by latent heat released by surrounding solidification. With the progress of solidification, the decreasing trend of melt temperature gradually slowed down, because a large amount of heat in the melt has been transferred to the mold, the temperature of the mold gradually increased, the temperature difference between the mold and the melt became smaller and smaller, and the heat transfer efficiency decreased significantly, delaying the further solidification process. The cooling capacity of Location *B*-3 was lower than that of Location *A*-3, and the cooling process of *C*-0 and *C*-1 was roughly the same. The cooling capacity of these six characteristic points was ranked as $D > C\text{-}0 \approx C\text{-}1 > C\text{-}2 > A\text{-}3 > B\text{-}3$. There was a great correlation between the solidification rate and the prediction of solidification defect generation. The changes in temperatures were disordered during the filling process, and they tended to be consistent around 610 ℃ after filling, as shown in Fig. 8(b).

As shown in Fig. 7(b), the structure of the component closely affected the solidification process, the heat released from the large planes or curved surfaces of the component could be transferred timely and effectively because the contact areas with the mold surfaces were large, and the cooling rate was fast. However, complex shape especially the deep concave cavity was not conducive to rapid solidification. The deep concave cavity of the component corresponded to the convex of mold, and the convex was surrounded by melt after filling, leading to the temperature rise. Thermal multidirectional input and single output inevitably led to heat accumulation, which delayed the process of solidification, and the solidification lag effect of the small-scale deep concave cavity structure was more significant. JEONG et al [4] simulated the solidification behavior of aluminum alloy automobile clutch housing, and the results showed that the solidification behavior began at the relatively thin zones in contact with the mold, while the solidification rate was slow at the relatively thick or curved zones due to the lack of heat dissipation. The solidification rule is similar to that obtained in this study. Similarly, the comparison of other simulation groups also conformed to the above rules.

3.3 Prediction of shrinkage cavity and shrinkage porosity defects

Shrinkage cavity and shrinkage porosity are common casting defects. The reason is that the volume difference caused by the solidification shrinkage of isolated liquid phase cannot be supplemented by the surrounding liquid phase. ProCAST software can predict the locations and quantities of shrinkage cavity and shrinkage porosity by the Niyama criterion.

Figure 9 shows the locations of shrinkage cavity and shrinkage porosity defects under different porosities. The porosity was defined by the volume fraction of pores in the units to the volume of these units to describe the type, volume, and severity of shrinkage cavity defects in flywheel housing components. Shrinkage cavity and shrinkage porosity appeared in the squeeze sprue and overflow grooves, which could reduce defects in the main body of the flywheel housing to a certain extent. Besides the sprue and overflow

grooves, obvious defects existed in the characteristic zones mentioned above, among which defects in *A*-2 and *B*-2 were smaller than those in other characteristic zones. And a few defects existed in the convex structures of the bottom surface and the top rounded surface of the component. In addition to the heat accumulation caused by the lag effect of solidification mentioned above, the complex shape of convex structure hindered the pressure transmission effect of the sprue feeding and forced feeding by local pressure.

The process of the indirect squeeze casting flywheel housing was a dynamic process in which the solidified shell was continuously thickened and shrunk, and the isostatic pressure acting on non-solidified alloy melt was continuously reduced [35]. The pressure acted on the alloy melt indirectly through the squeeze sprue. To intuitively describe the state of the alloy inside the flywheel housing, the solid fraction field during solidification is shown in Fig. 10.

When the overall solidification rate was low, as shown in Figs. 10(a−c), most of the alloy in the mold cavity was still liquid, the internal non-

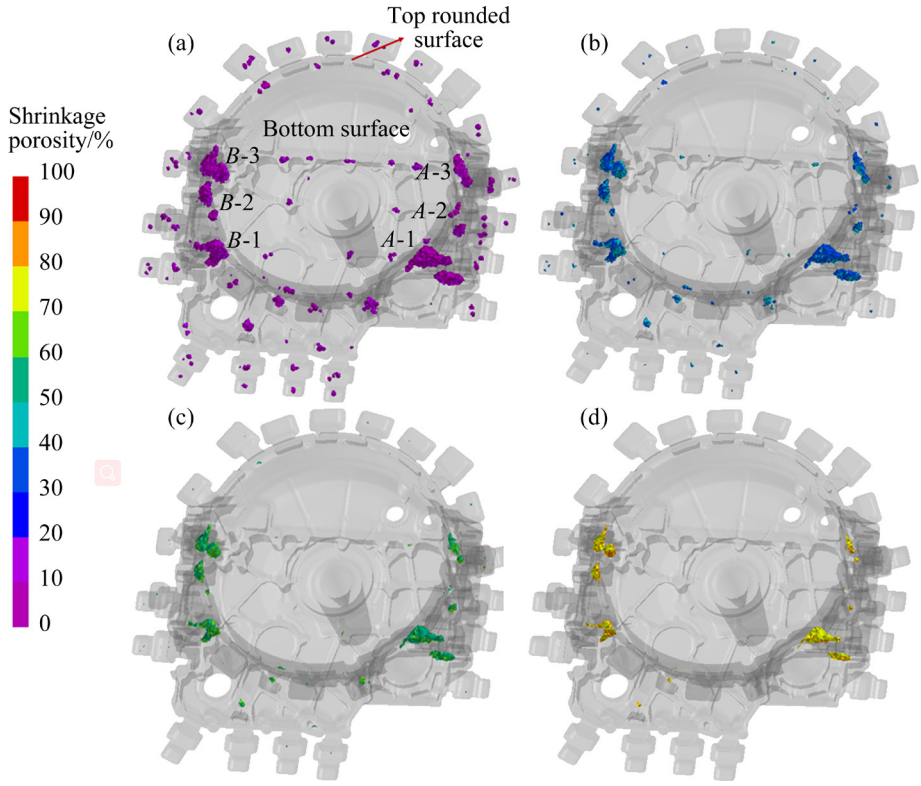

Fig. 9 Locations of shrinkage cavity and shrinkage porosity with porosity greater than 1% (a), 40% (b), 60% (c) and 80% (d)

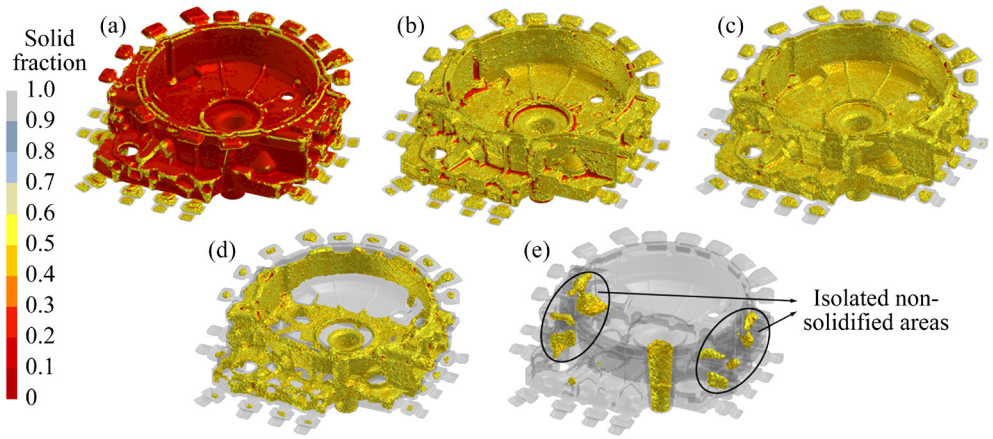

Fig. 10 Solid fraction field at overall solidification rate of 10% (a), 30% (b), 50% (c), 70% (d) and 90% (e)

solidified area was connected with the squeeze sprue as a whole, the pressure could be effectively transferred inside the liquid alloy, to ensure the close fit between the alloy and mold, the interfacial heat transfer increased sharply, and the hard solidified shell formed rapidly. As the solidification proceeded, it gradually transited from the periphery of the flywheel housing to the center, the thickness of the solidified shell increased continuously, the casting shrunk continuously, the heat transfer conditions deteriorated, and the interfacial heat transfer coefficient decreased gradually. When the overall solidification rate reached 70%, the good connection between the squeeze sprue and the internal non-solidified alloy began to be destroyed, as shown in Fig. 10(d). When it reached 90%, although the alloy in the sprue was not solidified to a state where the pressure cannot be transmitted at all, the feeding channel between the internal non-solidified areas and the sprue was completely disconnected, and multiple isolated non-solidified areas appeared, as shown in Fig. 10(e). In fact, these isolated areas were often the potential locations of the final defects, which were consistent with the locations of the shrinkage defects in Fig. 9.

The solidification process, pressure transfer, and heat transfer conditions were closely related. The experimental results of pressure transfer in squeeze casting by WANG et al [24] show that the measured pressure almost decreased linearly after it rapidly reached the peak value. The changing trend of the equivalent interface heat transfer coefficient set in this simulation was basically consistent with that of pressure measured by their experiments.

Due to the existence of friction, there will be pressure loss in the transmission of pressure from the pressurized locations to the far end. The farther the distance, the greater the pressure loss. The top rounded surface was far away from the sprue and local pressure locations, so the pressure loss was relatively large in the process of pressure transmission, and eventually, pressure for feeding was not enough. As a result, it led to shrinkage cavity and shrinkage porosity defects. LI et al [14] analyzed the numerical simulation results of squeeze casting of the automobile control arm. They reported that the feeding channel was blocked due to the first solidification of thin wall, and the locations of hot spots were difficult to be fed due to the distance from the sprue, which is similar to the analysis in this study.

To predict the possible locations and volume of defects as much as possible, porosity greater than 1% (the volume fraction of pore is greater than 1% of these units) was selected. The locations of defects in different simulation groups had a high similarity. And the volume of defects in different simulation groups was analyzed quantitatively, the minimum volume was 87.98 cm^3, and the maximum was 111.19 cm^3, as shown in Fig. 11. To determine the optimal combination of process parameters, range analysis was carried out with the volume of shrinkage porosity and shrinkage cavity defects as the judgment index. The calculation results are shown in Table 4.

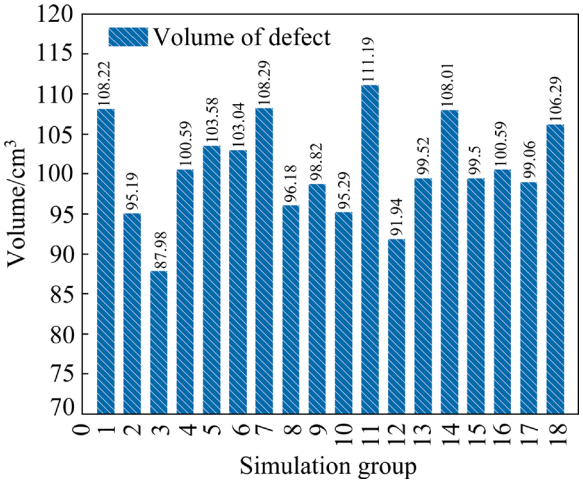

Fig. 11 Histogram of shrinkage cavity and shrinkage porosity volume in different simulation groups

According to the magnitude of the range (R), the order of the influence of each process parameter on the volume was local specific pressure > specific pressure > mold temperature > pouring temperature > pressure delay time. According to the magnitude of average value (k), the optimal combination of process parameters was determined, which involved pouring temperature of 650 °C, specific pressure of 48 MPa, mold temperature of 220 °C, local specific pressure of 800 MPa, and pressure delay time of 10 s (Side A) and 12 s (Side B).

3.4 Stress field during solidification

In the solidification process, due to the different solidification time, the component has different degrees of shrinkage, which will produce displacements in all directions. When the displacement is hindered by its structure or mold, it

Table 4 Volume of defects range analysis of orthogonal simulations at different levels

Level	Volume of defect/cm^3	R/cm^3
Pouring temperature $k1$	98.302	
Pouring temperature $k2$	101.710	3.408
Pouring temperature $k3$	101.372	
Specific pressure $k1$	102.087	
Specific pressure $k2$	102.035	4.825
Specific pressure $k3$	97.262	
Mold temperature $k1$	102.063	
Mold temperature $k2$	100.805	3.548
Mold temperature $k3$	98.515	
Local specific pressure $k1$	107.507	
Local specific pressure $k2$	96.938	10.569
Local specific pressure $k3$	96.938	
Pressure delay time $k1$	99.497	
Pressure delay time $k2$	100.698	1.691
Pressure delay time $k2$	101.188	

will lead to the generation of stress. If the stress exceeds the tensile strength of the material at a high temperature, plastic deformation or even cracking will occur. Simulation can judge the value and distribution of stress preliminarily.

Similarly, the simulation of the No. 3 component was taken as an example to analyze the displacement and stress field. The definition of the displacement here was the displacement of the nodes caused by solidification shrinkage. By observing the displacement field from Figs. 12(a) and (b), it can be found that there was no large displacement due to the obstruction of the mold and the mutual restriction of each part of the component, and the largest displacement was less than 0.05 cm. In addition, it could be clearly found that displacements at the thin walls were less than that at the thick walls from the displacement field of a section of the component in Fig. 12(c). Because the solidification shrinkage of aluminum alloy occurred from outside to inside and the inner displacement was hindered by the mold, the displacement of the periphery of the flywheel housing was greater than that of its interior. The locations with large displacements were the peripheries of overflow grooves and sprue. But, it had no effect on the dimension accuracy of the main body because these overflow grooves and sprue will be removed from the components in the following process.

The effective stress distribution can be observed by displaying different effective stresses in the cloud map in Figs. 13(a) to (d). The directions of the component were named as A, B, C, and D, respectively, as shown in Fig. 13(a). Figure 13(b) shows the effective stress values of 0−100 MPa, which were concentrated on both sides of A and B and the sprue. Figure 13(c) shows the concentration of effective stress values of 100−200 MPa in the horizontal plane, the thin wall on Side D, and some reinforced rib plates. The stress in the connecting section between the main body and each overflow groove was concentrated because there was a thickness mutation at both ends of these positions, but it had no effect on the main body of flywheel housing. The maximum effective

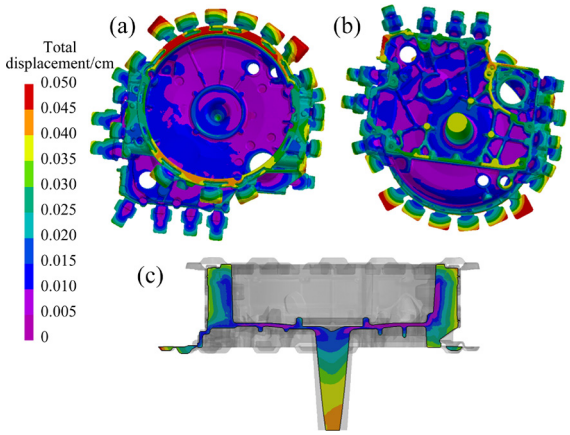

Fig. 12 Displacement field of No. 3 component: (a, b) Cloud maps; (c) Section

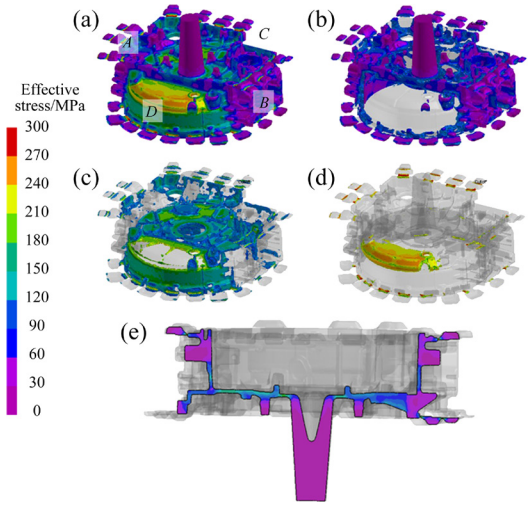

Fig. 13 Effective stress field of No.3 component: (a) Cloud map; (b) 0−100 MPa; (c) 100−200 MPa; (d) >200 MPa; (e) Section

stress occurred in the locations with fast cooling, thin wall, and large curvature, as shown in Fig. 13(d). By observing the stress field of a section of the component in Fig. 13(e), it could be obviously found that the effective stress value at the thin walls was higher than that at the thick walls, which was consistent with the above analysis.

To sum up, due to the nonuniform heat dissipation during solidification, the displacement and stress field showed a non-uniform distribution. The maximum stress during solidification occurred in the thin-walled structures with fast cooling rates and large curvature, while the stress values at the thick walls were not large. Given the plastic deformation or crack of the component, it is necessary to focus on the above zones. The distribution of effective stress in different simulation groups showed that the effective stress cloud maps had good consistency with some differences only in numerical values.

4 Process verification

To verify the reliability of the numerical simulation results, squeeze casting experiments of ZL104 aluminum alloy flywheel housing were carried out by using the process parameters of the above 18 schemes. Figure 14 shows the macro-photograph of formed components corresponding to each process scheme. The surfaces of all components were observed, and the surface quality was well. Silver metallic luster and the streamline of metal flow could be observed. The filling was complete, and no serious defects such as insufficient pouring and macroscopic crack were found. As shown in Fig. 15, the comparison between the simulated and experimental morphologies of sections at *A*-1, *B*-1, *A*-3, and *B*-3 locations of No. 1 flywheel housing indicated that

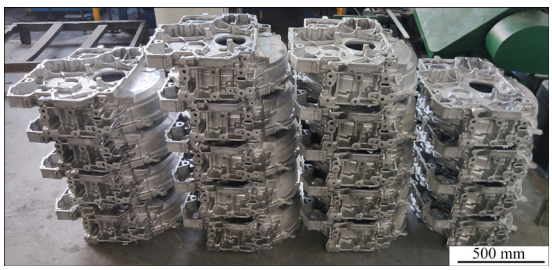

Fig. 14 Formed components corresponding to 18 groups of process schemes

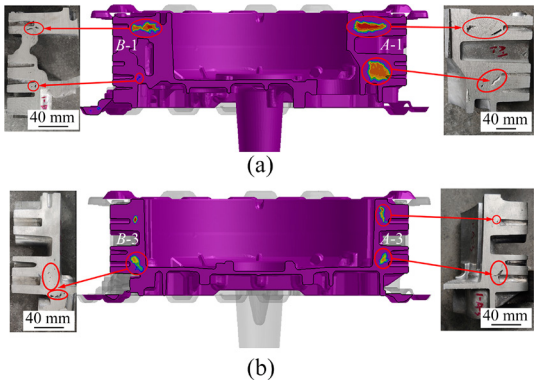

Fig. 15 Morphologies of sections at *A*-1 and *B*-1 (a), and *A*-3 and *B*-3 (b) locations of No.1 component

there were shrinkage cavity and shrinkage porosity defects at the locations predicted by the simulation, which verified the accuracy and reliability of this numerical simulation.

5 Conclusions

(1) The whole filling process was stable and could be divided into four stages: connection of small resistance channels, filling of horizontal zone with large resistance, filling of vertical direction, and filling of difficult-filling zone.

(2) There were six characteristic zones with obvious solidification lag. The geometry structure of the component closely affected the solidification process. Large flat and curved surfaces cooled rapidly. Complex shapes especially deep concave cavities were not conducive to rapid solidification, and the solidification lag effect of small-scale deep concave cavity structure was more significant.

(3) Shrinkage cavity and shrinkage porosity were obvious in the characteristic zones. In addition, the overflow grooves could transfer defects to a certain extent. According to range analysis of defects volume, the optimal combination of process parameters was determined as pouring temperature of 650 ℃, specific pressure of 48 MPa, mold temperature of 220 ℃, local specific pressure of 800 MPa, and pressure delay times of 10 s (Side *A*) and 12 s (Side *B*). The maximum effective stress occurred in the thin-walled structures with fast solidification and large curvature.

(4) Under 18 groups of the orthogonal experimental schemes, the flywheel housing components formed by squeeze casting were filled

completely and of good quality. The comparison between simulated and experimental morphologies of the same sections indicated that shrinkage cavity and shrinkage porosity existed in the locations predicted by this simulation, which validated the accuracy of prediction.

Acknowledgments

This work is supported by the National High Technology Research and Development Program of China (No. 2019YFB2006503), and the National Natural Science Foundation of China (No. 51875124).

References

[1] CHANG Xu-sheng, CHEN Gang, SUN Wei, ZHANG Hong-ming, CHU Guan-nan, ZHANG Xin, HAN Fei, ZHANG Wen-cong, DU Zhi-ming. Microstructures, mechanical properties and solidification mechanism of a hot tearing sensitive aluminum alloy asymmetric part fabricated by squeeze casting [J]. Journal of Alloys and Compounds, 2021, 886: 161254.

[2] QI Yu-shi, CHEN Li-li, CHEN Gang, LI Ke-feng, LI Chao, DU Zhi-ming. Preparation and properties of special vehicle cover via a novel squeeze casting quantitative feeding system of molten metal [J]. Metals, 2020, 10: 266.

[3] GHOMASHCHI M R, VIKHROV A. Squeeze casting: An overview [J]. Journal of Materials Processing Technology, 2000, 101: 1−9.

[4] JEONG S I, JIN C K, SEO H Y, KIM J D, KANG C G. Mold structure design and casting simulation of the high-pressure die casting for aluminum automotive clutch housing manufacturing [J]. The International Journal of Advanced Manufacturing Technology, 2016, 84: 1561−1572.

[5] YOU Dong-dong, WANG Xiang, CHENG Xue-yu, JIANG Xiao-mo. Friction modeling and analysis of injection process in squeeze casting [J]. Journal of Materials Processing Technology, 2017, 239: 42−51.

[6] KIAEE M, SULAIMAN S, TANG S H, MOHAMMADI M A. Investigation on microstructure and mechanical properties of squeeze cast Al−Si alloys by numerical simulation [J]. Advanced Materials Research, 2014, 1043: 31−35.

[7] MANJUNATH PATEL G C, MATHEW R, KRISHNA P, PARAPPAGOUDAR M B. Investigation of squeeze cast process parameters effects on secondary dendrite arm spacing using statistical regression and artificial neural network models [J]. Procedia Technology, 2014, 14: 149−156.

[8] WANG Yong-fei, ZHAO Sheng-dun, GUO Yi, YANG Jun-ling. Effects of process parameters on semi-solid squeeze casting performance of aluminum alloy scrolls for scroll compressors [J]. China Foundry, 2020, 17: 347−356.

[9] WANG Yong-fei, XING Shu-ming, AO Xiao-hui, GAO Wen-jing. Prediction model of rheological feeding distance under applied pressure [J]. International Journal of Metalcasting, 2021, 15: 1326−1339.

[10] HU Qi-yao, ZHAO Hai-dong, LONG Han, DONG Pu-yan, ZHU Gang. Numerical simulation of mold filling and particulate flow of A356/SiC_p indirect squeeze casting [J]. Journal of Composite Materials, 2020, 54: 1593−1602.

[11] SUN Zhi-zhong, HU H, NIU Xiao-ping. Experimental study and numerical verification of heat transfer in squeeze casting of aluminum alloy A443 [J]. Metallurgical and Materials Transactions B, 2012, 43: 1676−1683.

[12] KIM H H, KANG C G. Numerical simulation and experimental study for rheo-forged component using direct and indirect die system [J]. Transactions of Nonferrous Metals Society of China, 2010, 20: 1799−1804.

[13] LI Jun-hong, SUN Yu, WANG Yu, SUN Jue. Optimization of squeeze casting process of gearbox cover based on FEM and Box-Behnken design [J]. The International Journal of Advanced Manufacturing Technology, 2022, 118: 3421−3430.

[14] LI Yi-ze, YANG Hai-bo, XING Zhi-wei. Numerical simulation and process optimization of squeeze casting process of an automobile control arm [J]. The International Journal of Advanced Manufacturing Technology, 2017, 88: 941−947.

[15] WANG Fei-long, HAO Qiu-hong, YU Peng-fei, YANG Yu-jing, MA Ming-zhen, ZHANG Xin-yu, LIU Ri-ping. Numerical simulation and experimental verification of large-sized Zr-based bulk metallic glass ring-shaped parts in casting process [J]. Transactions of Nonferrous Metals Society of China, 2022, 32: 581−592.

[16] SOWA L, SKRZYPCZAK T, KWIATOŃ P. Analysis of temperature and velocity fields during filling of continuous casting mould [J]. Archives of Foundry Engineering, 2018, 18: 115−118.

[17] SOWA L, SKRZYPCZAK T, KWIATOŃ P. Influence of liquid metal movements on the casting creation [J]. Archives of Metallurgy and Materials, 2021, 66: 489−495.

[18] SOWA L, SKRZYPCZAK T, KWIATOŃ P. The Influence of riser shape on feeding effectiveness of solidifying casting [J]. Archives of Foundry Engineering, 2019, 19: 91−94.

[19] NZEBUKA G C, WAHEED M A. Thermal evolution in the direct chill casting of an Al−4pctCu alloy using the low-Reynolds number turbulence model [J]. International Journal of Thermal Sciences, 2020, 147: 106152.

[20] ZHANG Li-qiang, WANG Rong-ji. Estimation of heat flux at metal-mold interface during solidification of cylindrical casting [J]. International Journal of Material Forming, 2013, 6: 453−458.

[21] HU H, YU A. Numerical simulation of squeeze cast magnesium alloy AZ91D [J]. Modelling and Simulation in Materials Science and Engineering, 2002, 10: 1−11.

[22] YOU Dong-dong, SHAO Ming, LI Yuan-yuan, ZHOU Zhao-yao. Numerical simulation of mold-temperature-control solidification [J]. Transactions of Nonferrous Metals Society of China, 2007, 17: 443−448.

[23] LEWIS R W, POSTEK E W, HAN Zhi-qiang, GETHIN D T. A finite element model of the squeeze casting process [J]. International Journal of Numerical Methods for Heat & Fluid Flow, 2006, 16: 539−572.

[24] WANG Fei-fan, WANG Xu-yang, HAN Zhi-qiang. On the interfacial heat transfer and pressure transmission in squeeze

casting: A case study of the sensitivity to materials [J]. International Journal of Heat and Mass Transfer, 2019, 133: 52−61.
[25] NING Zhi-liang, ZHOU Bi-de, XUE Xiang, ZHANG Chun-hui. Numerical simulation of thermal stress field for die casting dies of aluminum alloy [J]. Transactions of Nonferrous Metals Society of China, 2000, 10: 650−652.
[26] ZHOU Bing, LU Shuai, XU Kai-le, XU Chun, WANG Zhan-yong, WANG Bin-jun. Hot cracking tendency test and simulation of 7075 semi-solid aluminium alloy [J]. Transactions of Nonferrous Metals Society of China, 2020, 30: 318−332.
[27] ZHOU Bo, WU Di, CHEN Rong-shi, HAN En-hou. Prediction of shrinkage microporosity in gravity-cast and low-pressure sand-cast Mg−6Gd−3Y−0.5Zr magnesium alloys [J]. Advanced Engineering Materials, 2019, 21: 1900755.
[28] LEE J H, KIM H S, WON C W, CANTOR B. Effect of the gap distance on the cooling behavior and the microstructure of indirect squeeze cast and gravity die cast 5083 wrought Al alloy [J]. Materials Science and Engineering A, 2002, 338: 182−190.
[29] WANG Fei-fan, WU Ke-yan, WANG Xu-yang, HAN Zhi-qiang. Measurement of temperature inside die and estimation of interfacial heat transfer coefficient in squeeze casting [J]. China Foundry, 2017, 14: 327−332.
[30] WANG Fei-fan, MA Qiang-xian, MENG Wen, HAN Zhi-qiang. Experimental study on the heat transfer behavior and contact pressure at the casting-mold interface in squeeze casting of aluminum alloy [J]. International Journal of Heat and Mass Transfer, 2017, 112: 1032−1043.
[31] ZHANG D L, CANTOR B. A numerical heat flow model for squeeze casting Al alloys and Al alloy/SiC_p composites [J]. Modelling and Simulation in Materials Science and Engineering, 1995, 3: 121−130.
[32] WANG Fei-fan, ZHAO Xue-ting, LIU Jia-hao, MA Qing-xian, SUB Jue, XU Shan-xin, HAN Zhi-qiang. Study on the relationship between interfacial heat transfer coefficient and interface pressure in squeeze casting by using microscopic contact model [J]. International Journal of Thermal Sciences, 2020, 152: 106300.
[33] XU Cai-ling, YING Fu-qing. Research on numerical simulation of filling velocity of indirect squeeze casting in shaping the thin walled workpiece [J]. Applied Mechanics and Materials, 2011, 48/49: 964−970.
[34] FARDI-ILKHCHY A, JABBARI M, DAVAMI P. Effect of pressure on heat transfer coefficient at the metal/mold interface of A356 aluminum alloy [J]. International Communications in Heat and Mass Transfer, 2012, 39: 705−712.
[35] LUO Shou-jing, JIANG Ju-fu, WANG Ying, TENG Dong-dong. Mechanics and forming theory of liquid metal forging [J]. Transactions of Nonferrous Metals Society of China, 2003, 13: 369−375.

大壁厚差复杂形状铝合金飞轮壳挤压铸造数值模拟

姜巨福[1]，葛 宁[1]，黄敏杰[1]，李明星[1]，王 迎[2]，丁长杰[3]，邹德超[3]

1. 哈尔滨工业大学 材料科学与工程学院，哈尔滨 150001；
2. 哈尔滨工业大学 机电工程学院，哈尔滨 150001；
3. 大连创新压铸件有限公司，大连 116600

摘 要：利用 ProCAST 软件对大壁厚差复杂形状 ZL104 铝合金飞轮壳挤压铸造过程进行数值模拟。结果表明：充型过程稳定且可分为 4 个阶段：流道连通、水平区域填充、竖直方向填充和难充填区填充。凝固过程中存在 6 个凝固滞后的特征区域，特征区域的缩孔缩松缺陷明显。缺陷位置预测准确，对预测的缺陷体积进行极差分析，确定最佳工艺参数为浇注温度 650 ℃、比压 48 MPa、模具温度 220 ℃、补压比压 800 MPa、补压延时 10 s(*A* 侧)和 12 s(*B* 侧)。最大铸造应力出现在凝固速度快、曲率大的薄壁结构中。仿真结果得到了实际工艺验证。

关键词：数值模拟；挤压铸造；大壁厚差；复杂形状；定域补压

(Edited by Xiang-qun LI)